Journal of Electronic Materials (2022) 51:4666–4674
https://doi.org/10.1007/s11664-022-09561-3

2021 U.S. WORKSHOP ON PHYSICS AND CHEMISTRY OF II-VI MATERIALS

Long and Very Long Wavelength InAs/InAsSb Superlattice Complementary Barrier Infrared Detectors

David Z. Ting[1] · Arezou Khoshakhlagh[1] · Alexander Soibel[1] · Sam A. Keo[1] · Anita M. Fisher[1] · Brian J. Pepper[1] · Linda Höglund[1,2] · Sir B. Rafol[1] · Cory J. Hill[1] · Sarath D. Gunapala[1]

Received: 3 November 2021 / Accepted: 28 February 2022 / Published online: 23 March 2022

Abstract
While the *n*-type InAs/InAsSb type-II strained layer superlattice (T2SLS) has demonstrated excellent detector and focal plane array performance in the mid-wavelength infrared, it is limited in its attainable quantum efficiency (QE) in the long and very long wavelength infrared due to short hole diffusion length and modest absorption coefficient. We explore InAs/InAsSb T2SLS unipolar barrier infrared detectors that contain *p*-type absorber layers in order to take advantage of the longer electron diffusion length for QE enhancement. We find that while they can achieve enhanced QE, their dark current characteristics are affected by the presence of metallurgical and surface *p*-*n* junctions, and are best operated under lower biasing conditions where the tunneling dark currents are less pronounced. We report results on complementary barrier infrared detector structures that use *n*-type absorbers, a combination of *p*- and *n*-type absorbers, and *p*-type absorbers, with cutoff wavelengths ranging from 10.0 µm to 15.3 µm.

Keywords Infrared detector · unipolar barrier · type-II superlattice · InAs/InAsSb superlattice

Introduction

The InAs/InAsSb (gallium-free) type-II strained-layer superlattice (T2SLS) has emerged as a viable infrared detector material that is actively explored by research groups worldwide.[1–9] Compared to the more established InAs/GaSb type-II superlattice (T2SL), it is easier to grow[8] and has demonstrated longer minority carrier lifetimes.[10–12] Mid-wavelength infrared (MWIR) focal plane arrays (FPAs) based on the InAs/InAsSb T2SLS *n*B*n* detector[13,14] have demonstrated significantly higher operating temperature than their InSb counterparts while retaining the same III-V semiconductor manufacturability benefits, thus establishing the InAs/InAsSb T2SLS as an important infrared detector material.

One disadvantage of InAs/InAsSb is that it requires a longer superlattice period to achieve long or very long wavelength cutoffs when compared to InAs/GaSb. Figure 1 plots the cutoff wavelength (as derived from calculated superlattice band gap) as a function of superlattice period for a set of InAs/InAsSb and a set of InAs/GaSb superlattices. In the MWIR, the two sets show comparable periods. But as the cutoff wavelength increases, the periodicity disadvantage (i.e., requiring longer period to achieve the same cutoff wavelength) of the Ga-free superlattice becomes apparent. The longer period in the Ga-free superlattice results in weaker electron-hole wavefunction overlap and smaller absorption coefficient.[15,16] Therefore, a thicker absorber is needed to achieve good quantum efficiency (QE). At the same time, a longer period also means a larger separation between the hole quantum wells, which leads to larger hole effective masses. Figure 2 shows the calculated conductivity effective masses[17,18] for the same two sets of superlattices. In the long wavelength infrared (LWIR) and very long wavelength infrared (VLWIR) the InAs/InAsSb T2SLS has larger growth-direction hole conductivity effective mass ($m_{p,z}^{**}$) compared to the InAs/GaSb T2SL, and with $m_{p,z}^{**}$ increasing rapidly with the cutoff wavelength. The diffusion length is inversely proportional to the square root of the conductivity effective mass.[17] Short diffusion length limits the absorber

✉ David Z. Ting
David.Z.Ting@jpl.nasa.gov

[1] Jet Propulsion Laboratory, California Institute of Technology, M/S 302-231, 4800 Oak Grove Drive, Pasadena, CA 91109-8099, USA

[2] Present Address: IRnova AB, Stockholm, Sweden

thickness, and in turn limits the attainable QE. This is unfavorable for (V)LWIR Ga-free superlattice detectors based on the *n*B*n*[19] or XB*n*[20] designs, which rely on hole transport in *n*-type absorber. To continue to benefit from the known advantages of the *n*B*n*/XB*n* into the (V)LWIR without significant sacrifice in QE, ideas for increasing the absorption coefficients of the Ga-free superlattice have been explored. They include the use of higher Sb fraction, polytype superlattices, and metamorphic buffers, all of which were found to involve substantial trade-offs.[21] Figure 2 also shows that the growth-direction electron conductivity effective mass ($m_{n,z}^{**}$) for both sets of superlattice remain quite small even for (V)LWIR cutoff wavelengths. This suggests that the longer electron diffusion length in the *p*-type Ga-free superlattice can be exploited to achieve higher QE.

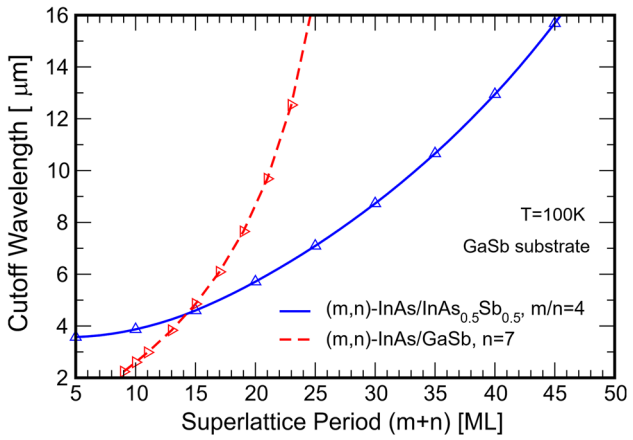

Fig. 1 Calculated cutoff wavelength for the (*m*,*n*)-InAs/$InAs_{0.5}Sb_{0.5}$ superlattices with *m*/*n*=4, and for the (*m*,*n*)-InAs/GaSb superlattices with *n*=7, as functions of superlattice period in monolayers (MLs).

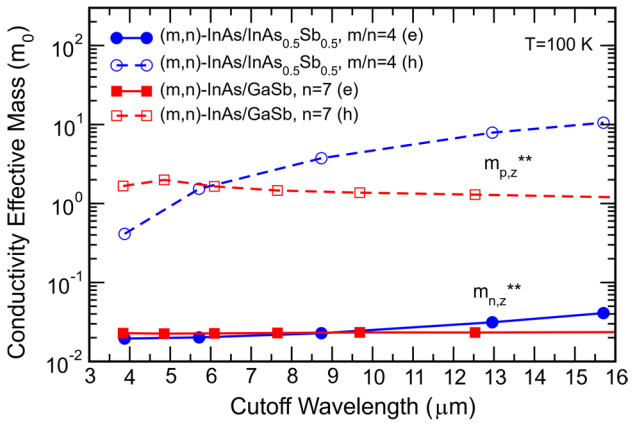

Fig. 2 Growth-direction electron conductivity effective mass $m_{n,z}^{**}$ and hole conductivity effective mass $m_{p,z}^{**}$ as function of cutoff wavelength for the (*m*,*n*)-InAs/$InAs_{0.5}Sb_{0.5}$ superlattices with *m*/*n*=4, and for the (*m*,*n*)-InAs/GaSb superlattices with *n*=7.

Detector Architectures for Enhancing LWIR Superlattice Quantum Efficiency

In this section we discuss device architectures for (V)LWIR InAs/InAsSb T2SLS detectors. An important aspect for (V)LWIR detectors is the management of surface-related dark currents; extensive discussions on the subject as related to antimonide-based detectors can be found in the references by Sidor, Savich, and Wicks.[22,23] While QE in (V)LWIR InAs/InAsSb T2SLS *n*B*n* detectors are limited by their short hole diffusion lengths, the *n*B*n* architecture still has important advantages so that they should not be dismissed readily. The simple *n*B*n* structure can suppress generation-recombination (G-R) and surface dark currents. As pointed out by Maimon and Wicks,[19] an *n*B*n* pixel can be defined by etching to (but not through) the barrier, leaving the active absorber layer covered by the wide band gap barrier layer. With no exposed absorber surface, there is no need for additional surface passivation. Even when an *nBn* pixel is fully reticulated, the surface leakage current path is blocked by the electron barrier.[23] For the case of the InAs/InAsSb T2SLS, the exposed absorber side wall surface is degenerate *n*-type. As illustrated in Fig. 3, the accumulated surface potential repels the minority carriers (holes) from the etched absorber surface, which consequently is relatively benign.

We can enhance the *n*B*n* (or XB*n*) QE performance by introducing band gap grading in the absorber layer, as illustrated in Fig. 4. For the InAs/InAsSb T2SLS, this is easily accomplished by gradually varying the absorber superlattice period. This results in a built-in quasi-electric field that facilitates hole transport through drift. With better hole transport, we can increase the absorber thickness for improved QE. We note that a steeper grading results in a stronger field, but with the trade-off of a more gradual photoresponse cutoff.

An alternative option for addressing the (V)LWIR QE problem is to turn to *p*-type absorbers, which provide longer (electron) diffusion lengths. The simplest *p*-type unipolar

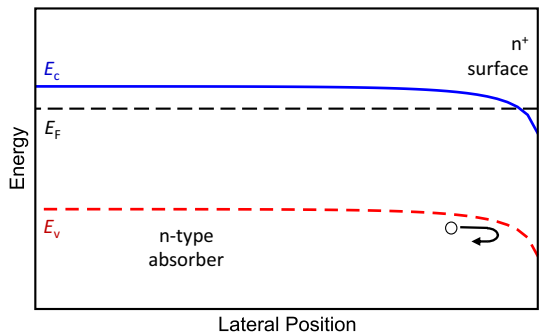

Fig. 3 Energy band diagram illustrating band bending near the surface of an *n*-type InAs/InAsSb T2SLS. The surface is degenerate *n*-type.

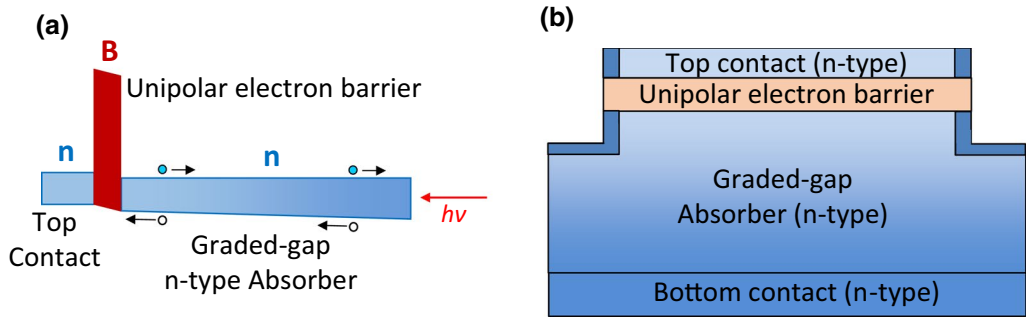

Fig. 4 (a) Schematic energy band diagram and (b) layer structure layer diagram of an *n*B*n* detector with a graded band gap absorber. The device is designed for top-negative bias (*p*-on-*n*) operation.

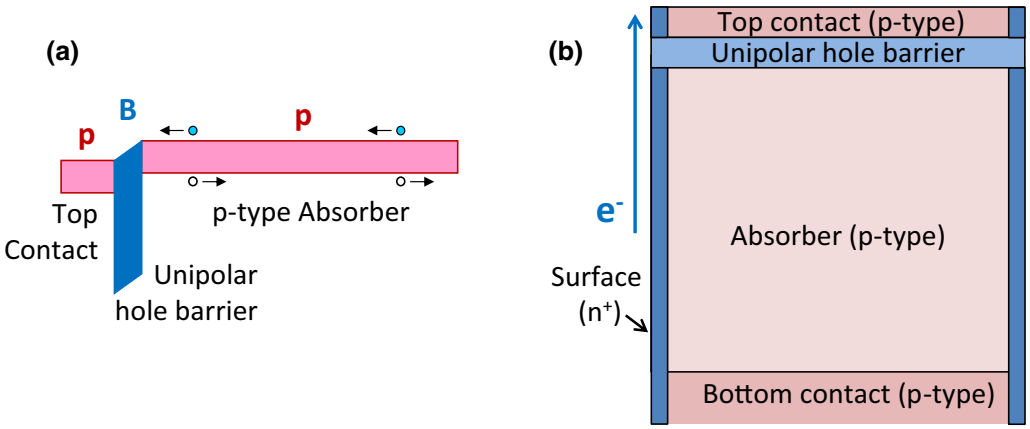

Fig. 5 (a) Schematic energy band diagram and (b) layer structure diagram of a *p*B*p* detector. Note that the device is designed for top-positive bias (*n*-on-*p*) operation.

barrier detector structure is the *p*B*p* or XB*p*.[24,25] The *p*B*p* is the analogue of the *n*B*n*, but with a *p*-type top contact, a unipolar hole barrier, and a *p*-type absorber, as illustrated in Fig. 5. The *p*B*p* has already been implemented for (V) LWIR InAs/GaSb T2SL absorbers.[26,27] The problem with the Ga-free superlattice *p*B*p* is that the surface of *p*-type InAs/InAsSb superlattice inverts to degenerate *n*-type and provides a shunt current path that is not blocked by the unipolar hole barrier, as illustrated in Fig. 5b. As a result, there is large electron surface leakage dark current (sidewall shunt current). The inverted surface is problematic in another way. As illustrated in Fig. 6, the degenerate *n*-type surface creates a surface *p*-*n* junction with a sub-surface depletion region,[22] and is subject to various surface dark current mechanisms.[28]

The complementary barrier infrared detector (CBIRD) architecture [29, 30] can be used to address the surface shunt current problem.[23] The CBIRD structure consists of an absorber surrounded on the two sides by a pair of complementary unipolar electron and hole barriers, and capped at the two ends with top and bottom contact layers. The CBIRD absorber can be *n*-type (*n*-CBIRD) or *p*-type (*p*-CBIRD); Fig. 7a shows the schematic band diagram for a *p*-CBIRD

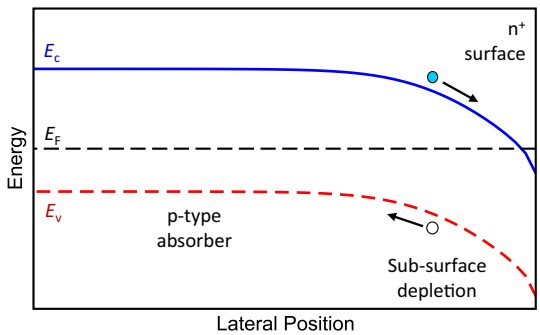

Fig. 6 Energy band diagram illustrating band bending near the surface of a *p*-type InAs/InAsSb T2SLS. The surface is degenerate *n*-type.

structure. CBIRD was originally implemented for *p*-type InAs/GaSb T2SL, with an InAs/GaSb T2SL electron barrier and an InAs/AlSb superlattice hole barrier.[29,30] For a CBIRD with an InAs/InAsSb T2SLS absorber, we can use a shorter-period (larger band gap) InAs/InAsSb T2SLS as the unipolar hole barrier, since the conduction bands of different InAs/InAsSb superlattices are always approximately

aligned; we can also use AlGaAsSb as the unipolar electron barrier, as has been done for the MWIR InAs/InAsSb T2SLS *n*B*n*.[13,14] As illustrated in Fig. 7b, although the surface of *p*-type InAs/InAsSb T2SLS inverts to degenerate *n*-type, the electron surface leakage path is interrupted by the electron unipolar barrier.

As illustrated in Fig. 7b, for detector mesa isolation the *p*-CBIRD requires etching past the *p*-absorber to the bottom n-contact, thus creating exposed superlattice absorber sidewall surfaces. Even though the unipolar barriers in the CBIRD can block surface shunt current, the inverted surface of *p*-absorber is still problematic for CBIRD because the barriers cannot block dark currents generated at the surface *p*-*n* junction. An example given by Sidor et al.[23] is surface G-R dark current. Figure 6 shows that for an electron-hole pair generated in the sub-surface depletion region, the electron is driven to the n^+ surface and then flows along the surface toward the bottom contact, and the hole enters the bulk *p*-absorber region and flows toward the top contact; neither are blocked by the two unipolar barriers.

The inverted surface dark current problem can be mitigated to some degree by considering a CBIRD structure that incorporates both *p*-type and *n*-type absorber sections.[31,32] Figure 8 illustrates such a structure, which is identical to the *p*-CBIRD of Fig. 7, except that the bottom portion of the *p*-type absorber is replaced by an *n*-type absorber layer. In this *pn*-CBIRD structure the detector pixel is delineated by etching through the *p*-type absorber layer, past the *p*-*n* junction and into the *n*-type absorber layer. The exposed *n*-type absorber surface, which is also degenerate *n*-type, is relatively benign since there is no sub-surface *p*-*n* junction. Meanwhile, we have reduced the area of the *p*-type absorber sidewall surface and the associated dark currents. The general philosophy is to construct the absorber with as thick an *n*-type absorber layer as the hole diffusion length would permit, and then add onto it a *p*-type layer with the minimum thickness necessary to achieve the desired QE. In this way we can minimize the etch depth and the exposed *p*-absorber surface area. It is noted that the *pn*-CBIRD contains a *p*-*n* homojunction (a feature that the *n*B*n* avoids explicitly) and

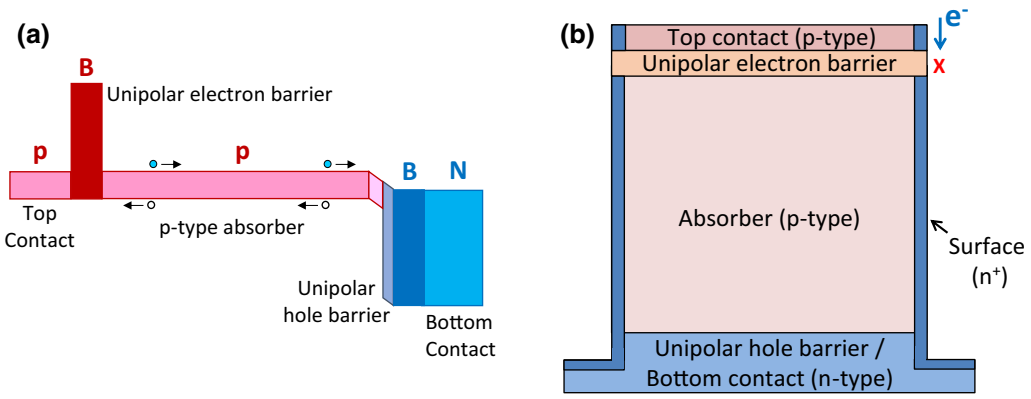

Fig. 7 (a) Schematic energy band diagram and (b) layer structure diagram of a complementary barrier infrared detector with *p*-type absorber (*p*-CBIRD).

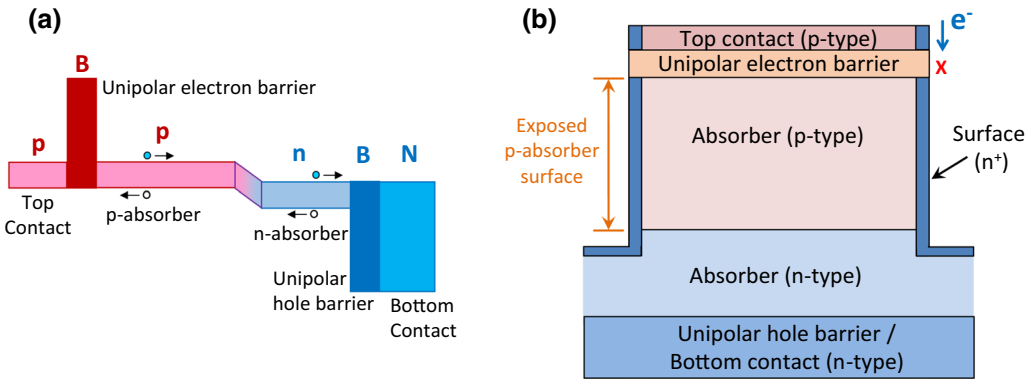

Fig. 8 (a) Schematic energy band diagram and (b) layer structure diagram of a complementary barrier infrared detector with *p*-type and *n*-type absorber sections (*pn*-CBIRD).

that the pixel etch exposes the sidewall of this *p-n* junction. In general, both the *pn*-CBIRD and *p*-CBIRD benefit from surface passivation.

It is instructive to compare the *pn*-CBIRD with a simple *p-n* junction device. Both are subject to *p-n* homojunction G-R dark current. The *pn*-CBIRD benefits from reduced minority carrier injection from the contact layers due to the presence of the electron and hole barriers. However, the main advantage of the *pn*-CBIRD is that the electron surface leakage path is interrupted by the electron unipolar barrier, as illustrated in Fig. 8b. This is reminiscent of the comparison between the InAs *n*B*n* and *p-n* junction photodetectors; while the InAs *n*B*n* benefits from G-R suppression, its main advantage over the InAs *p-n* junction is surface leakage current suppression.[33]

Device Results

We first examine results for LWIR InAs/InAsSb T2SLS CBIRD structures. Sb3001 is an *n*-CBIRD with a 3.2-μm-thick graded-gap *n*-type superlattice absorber. Sb3002 and Sb3003 are both *pn*-CBIRDs, each with a 2.5-μm-thick *p*-type non-graded absorber plus the same 3.2-μm-thick graded-gap *n*-type absorber as in Sb3001. The structures of Sb3001 and Sb3002 are described in detail in Ref. 32, and the structure of Sb3003 is nominally the same as Sb3002. Figure 9 shows the spectral QE measured under −0.15 V bias at 77 K for Sb3001, Sb3002, and Sb3003, with cutoff wavelengths of 10.0 μm, 10.3 μm, and 10.4 μm, respectively. The higher QE in the *pn*-CBIRD samples Sb3002 and Sb3003 are attributed to the additional *p*-type absorber layer. The inset shows the 77 K QE at 8.6 μm as functions of applied bias for the three devices; all three devices have zero-bias turn on. Figure 10 shows the measured dark current density as a function of applied bias (*J-V*) for Sb3003 for temperatures ranging from 78 K to 148 K. Arrhenius analysis (not shown) indicates an activation energy of 0.097 eV at -0.1 V bias over this temperature range, compared to a band gap of 0.119 eV estimated from the 10.4-μm cutoff wavelength. The corresponding dark current results for Sb3001 and Sb3002 can be found in Ref. 32. In general, the dark current characteristics for all three samples are fairly well behaved under lower bias in this temperature range. Figure 11 shows the dark current density as a function of temperature (40 K to 148 K) at applied bias ranging from −0.1 V to −0.7 V for Sb3001 and Sb3002. At lower temperature and higher bias, the presence of tunneling current is very apparent for both the *n*-CBIRD sample Sb3001 and the *pn*-CBIRD sample Sb3002. Additional results on Sb3001 and Sb3002 can be found in Ref. 32.

We next look at two VLWIR CBIRD samples. Sb3019 is a *pn*-CBIRD with a 2.5-μm-thick *p*-type non-graded absorber plus a 2.5-μm-thick graded-gap *n*-type absorber, and Sb3021 is a *p*-CBIRD with a 5-μm-thick *p*-type non-graded absorber; the structure details are described in Ref.32 Figure 12a shows the spectral QE measured under -0.3 V bias at 60 K for Sb3019 and Sb3021, with cutoff wavelengths of 13.3 μm, and 12.1 μm, respectively. Both samples show reasonably good QE under these conditions. The inset shows the 60 K QE at 8.6 μm as functions of applied bias. Sb3019 has a turn on bias of ~ -0.15 V, while Sb3021 shows zero turn-on bias. Figure 12b shows the QE at 10 μm as a function of temperature. For the *p*-CBIRD sample Sb3021, the

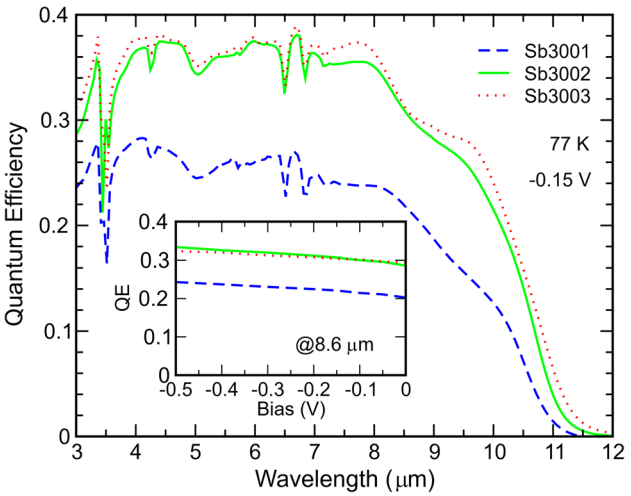

Fig. 9 Backside illuminated spectral QE for non-anti-reflection coated detectors fabricated from samples Sb3001, Sb3002, and Sb3003, measured under -0.15 V bias at 77 K. The inset shows the QE at 8.6 μm as a function of applied bias.

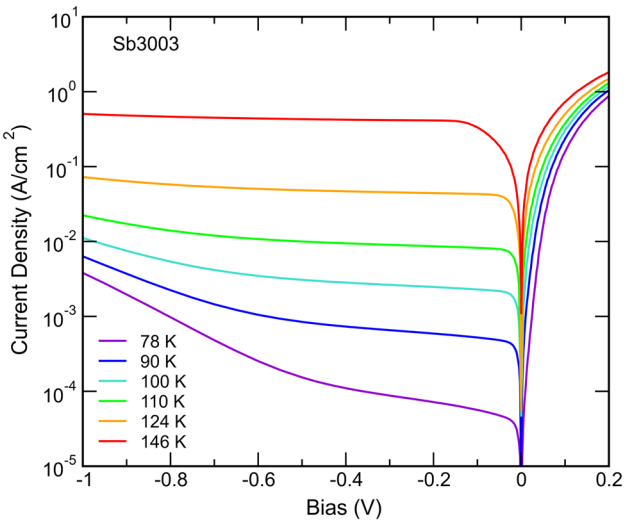

Fig. 10 Dark current density as a function of applied bias, measured at temperatures ranging from 78 K to 146 K for a *pn*-CBIRD detector fabricated from sample Sb3003.

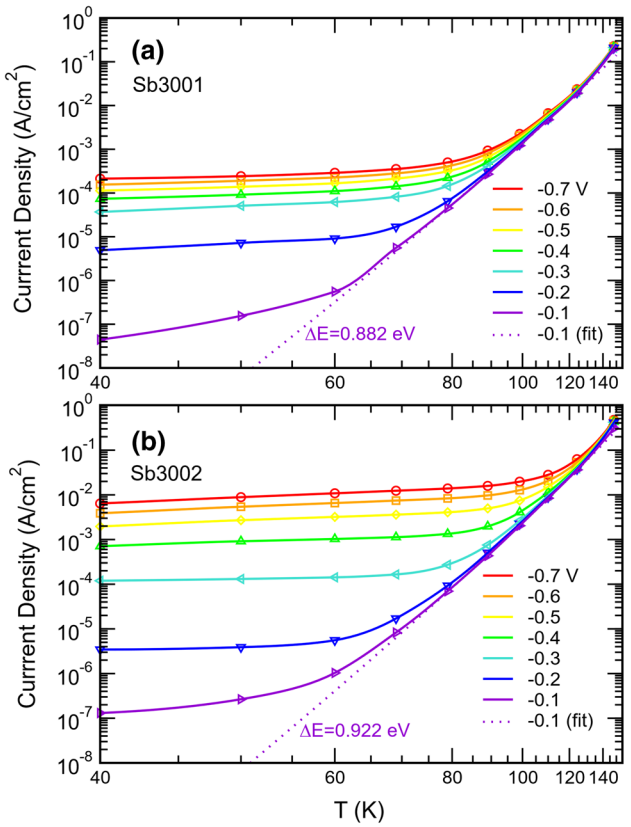

Fig. 11 Dark current density as a function of temperature, measured under reverse bias ranging from −0.1 V to -0.7 V for (a) an *n*-CBIRD detector fabricated from Sb3001, and (b) a *pn*-CBIRD detector fabricated from Sb3002. Arrhenius fit for the -0.1 V case is shown as dotted line.

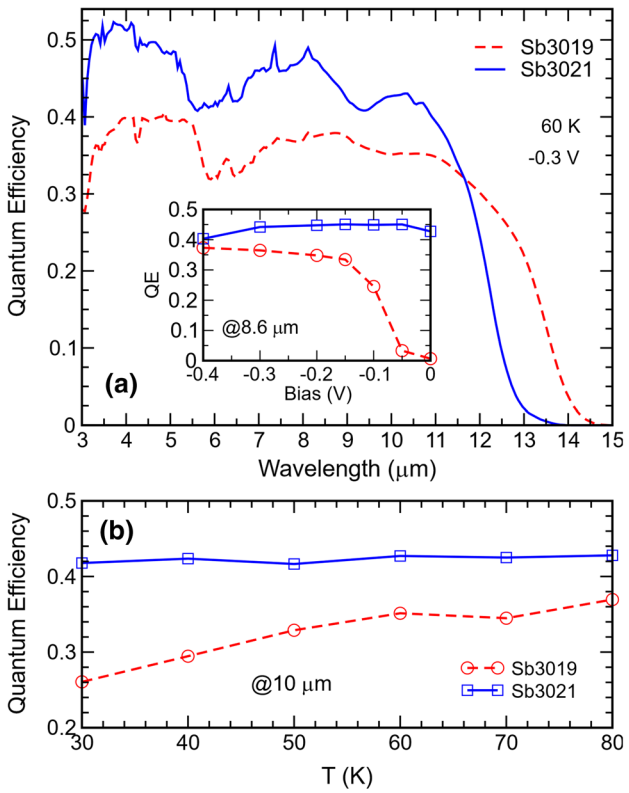

Fig. 12 (a) Backside illuminated spectral QE for non-anti-reflection coated detectors fabricated from Sb3019 and Sb3021, measured under -0.3 V bias at 80 K. The inset shows QE at 8.6 μm as a function of applied bias. (b) QE at 10 μm as a function of temperature for Sb3019 and Sb3021.

QE remains fairly constant as we lower the temperature from 80 K to 30 K. For the *pn*-CBIRD sample Sb3019, however, we see a monotonic QE drop as the temperature is lowered over the same range. The fact that QE remains basically the same for the *p*-CBIRD suggests that the electron diffusion length for the *p*-type absorber in the 30 K to 80 K range is at least 5 μm. This also suggests that for *pn*-CBIRD the minority carrier (electron) transport in the 2.5-μm-thick *p*-type absorber is not limited by the electron diffusion length and that the reduction in QE with temperature drop is due to the decrease in the *n*-type absorber hole diffusion length, which appears to be no more than 2.5 μm in the 30 K to 80 K range. Figure 13 shows the measured dark *J*-*V* characteristics of Sb3019 and Sb3021 at temperatures ranging from 30 K to 148 K. For both, the presence of tunneling dark current is very apparent in the *J*-*V* characteristics at lower temperatures and higher biases. The −0.15 V dark current density values for Sb3019 and Sb3021 at 60 K are 6.6×10^{-5} A/cm^2 and 7.6×10^{-5} A/cm^2, which are factors of ~13.5 and ~92 higher than predicted by the MCT Rule 07[8] for their respective cutoff wavelengths. Arrhenius analysis of dark current at −0.2 V bias indicates a mixture of diffusion and G-R dark current components in the 89 K to 123 K range, a mixture of G-R and tunneling dark currents in the 60 K to 79 K range, and strong tunneling dark current at below 50 K.[32] A demonstration FPA made from the 13.3-μm cutoff *pn*-CBIRD sample Sb3019 showed good operability; the results were briefly reported in Ref. 32, along with additional detector results on Sb3019 and Sb3021.

We have seen signs of tunneling dark current in the *n*-CBIRD, the *pn*-CBIRD, and the p-CIBRD at lower temperatures and higher biases. Modeling results in Fig. 14 show the energy band diagrams for the three types of CBIRDs under 0 and -0.4 V bias; an absorber band gap of ~0.1 eV is used in the modeling. For the *n*-CBIRD, the doping levels of top contact, electron barrier, absorber, hole barrier, and bottom contact are, respectively, $p=3\times10^{17}$, $P=2\times10^{16}$, $n=1\times10^{15}$, $N=1\times10^{15}$, and $N=1\times10^{17}$ cm^{-3}; for the *pn*-CBIRD and *p*-CBIRD, the *p*-type absorber doping is $p=3\times10^{15}$ cm^{-3}. Figure 14 shows that the applied bias drops mainly at the electron-barrier/absorber junction for the *n*-CBIRD, at the absorber *p*-*n* homojunction for the *pn*-CBIRD, and at the absorber/hole-barrier junction for the

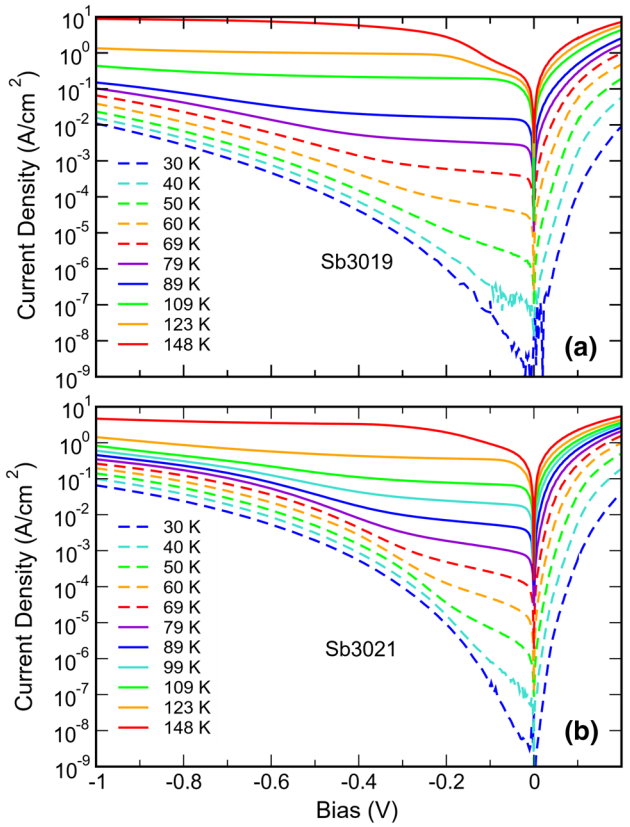

Fig. 13 Dark current density as a function of applied bias, measured at temperatures ranging from 30 K to 148 K for (a) a *pn*-CBIRD detector fabricated from Sb3019, and (b) a *p*-CBIRD detector fabricated from Sb3021.

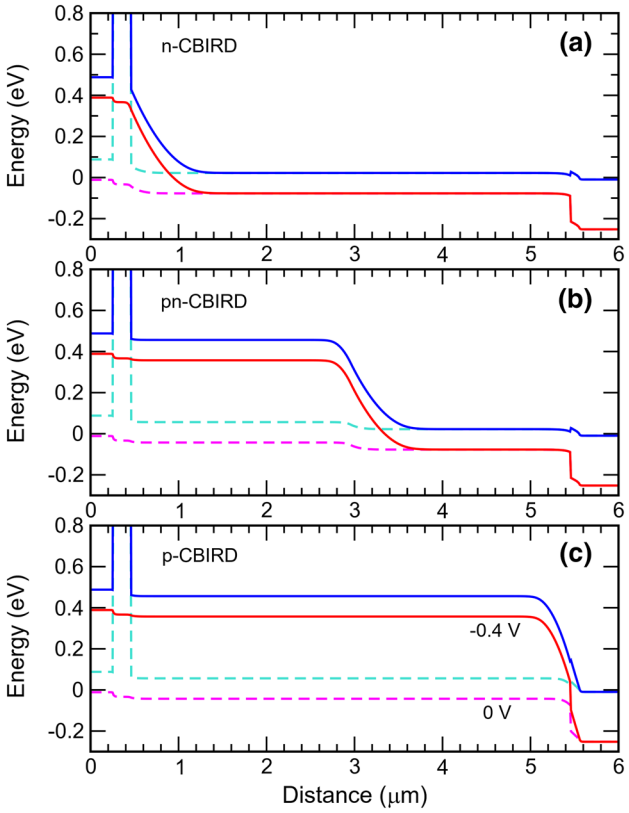

Fig. 14 Energy band diagrams for (a) *n*-CBIRD, (b) *pn*-CBIRD, and (c) *p*-CBIRD under 0 and -0.4 V bias. The absorber band gap is 0.099 eV, corresponding to 12.5-μm cutoff wavelength.

p-CBIRD. In all cases, because of the narrow (V)LWIR absorber band gap (0.1 eV in this case), even a modest bias (−0.4 V in this case) can produce band bending that is very favorable for tunneling. In addition, for *p*-type absorber with an inverted n^+ surface, the surface *p*-*n* junction could also be a source for tunneling dark current. To be sure, the energy gap that is relevant for tunneling in superlattices is the conduction band/light-hole gap ($E_{c1} - E_{lh1}$), which is ~2.5 times the fundamental superlattice band gap ($E_{c1} - E_{hh1}$) in this case.[17] Nevertheless, this energy gap is still quite small and is susceptible to tunneling under moderate bias. For the *n*-CBIRD and the *p*-CBIRD, it should be possible to alleviate the tunneling problem somewhat by adjusting the doping profile at and near the barrier, or by placing the electrical junction in the wide-gap barrier region away from the metallurgical barrier/absorber heterojunction.[30] In the case of the *n*-CBIRD, having an undoped electron barrier would increase the fraction of bias drop in the barrier, and decrease the bias drop in the narrow gap absorber region for reduced tunneling under higher reverse bias.

Finally, we examine a *pn*-CBIRD with an even longer cutoff wavelength. Sb3816 is a *pn*-CBIRD with a ~2.8-μm-thick *p*-type absorber plus a ~1.8-μm-thick *n*-type non-graded InAs/InAsSb T2SLS absorber, with an AlGaAsSb electron barrier and a shorter-period InAs/InAsSb superlattice hole barrier. Figure 15 shows the spectral QE measured under −0.1 V bias at 60 K for Sb3816; the cutoff wavelength is ~15.3 μm. The inflection point near the spectral QE cutoff puts the estimated band gap[34] at 0.0789 eV (~15.7 μm). The inset shows the 60 K QE at 8.6 μm as a function of applied bias; the turn-on bias is <50 mV. Figure 16 shows the *J*-*V* characteristics for Sb3816 for temperatures ranging from 40 K to 99 K. Arrhenius analysis in the inset indicates an activation energy of 0.063 eV at −0.1 V bias in the 60 K to 99 K temperature range. The −0.1 V dark current density at 50 K is 1.15×10^{-4} A/cm^2, which is a factor of ~24 higher than predicted by the MCT Rule 07[35] for the estimated band gap. Overall, even at this very long cutoff wavelength, the *pn*-CBIRD appears to be fairly well behaved.

Summary

While the *n*-type InAs/InAsSb T2SLS has demonstrated excellent detector and FPA performance in the MWIR, it is limited in its attainable QE in the (V)LWIR due to short hole

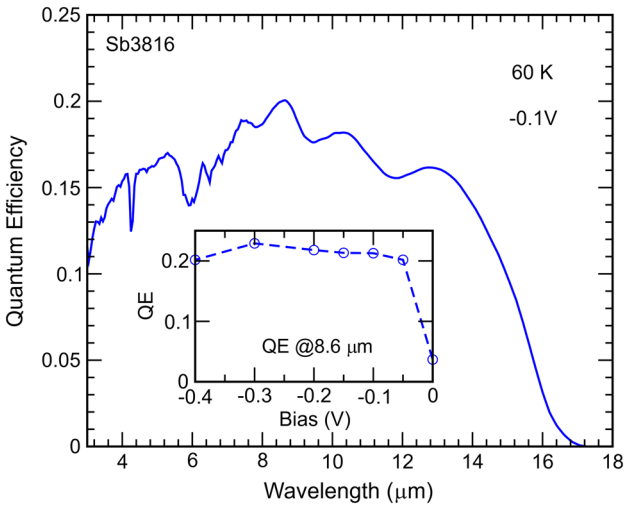

Fig. 15 Backside illuminated spectral QE for non-anti-reflection coated detectors fabricated from Sb3816, measured under −0.1 V bias at 60 K. The inset shows the QE at 8.6 μm as a function of applied bias.

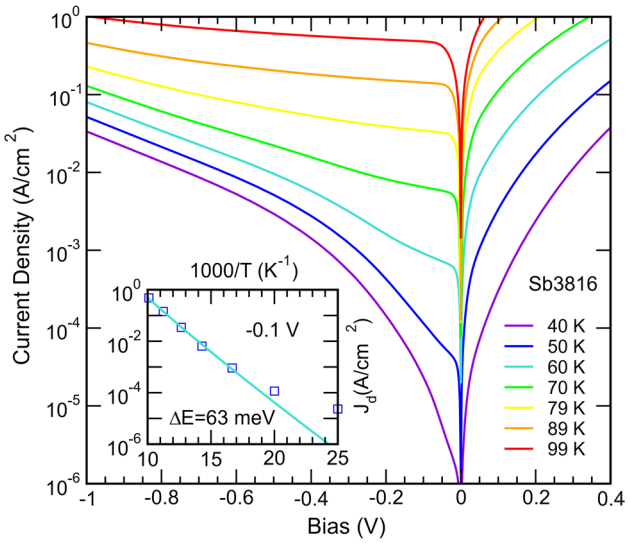

Fig. 16 Dark current density (J_d) as a function of applied bias, measured at temperatures ranging from 40 K to 99 K for a VLWIR detector fabricated from Sb3816. The insets show J_d temperature dependence at −0.1 V bias, labeled with the activation energy from Arrhenius analysis.

diffusion length and modest absorption coefficient. A graded band gap can be used to enhance hole transport in *n*-type absorber, and the longer electron diffusion length in *p*-type absorber can also be exploited for achieving higher QE. Mesa etch for pixel delineation typically expose absorber sidewall surfaces. If not well-passivated, this could be problematic for the InAs/InAsSb T2SLS absorber. The exposed InAs/InAsSb T2SLS absorber surface is degenerate *n*-type, and can lead to surface shunt current, which, fortunately, can be suppressed effectively by using a device architecture like the CBIRD. A detector array based on CBIRD with *p*-type InAs/InAsSb T2SL absorber requires a deep mesa etch that exposes the surface of the entire absorber section; the exposed surface is subject to the deleterious effects of surface *p*-*n* junction and surface defects. Rather than using *p*-type absorber only, a CBIRD with a combination of *p*- and *n*-type absorber sections can benefit from a shallower mesa etch that reduces fabrication demands and also decreases the *p*-type absorber exposed surface area. We report results on CBIRD structures that use graded *n*-type absorber, a combination of *p*- and *n*-type absorbers, and *p*-type absorber, with cutoff wavelengths ranging from 10.0 μm to 15.3 μm. We find the (V)LWIR CBIRD dark current characteristics are affected by the presence of metallurgical and surface *p*-*n* junctions, and are best operated under lower biasing conditions where the tunneling dark currents are less pronounced.

Acknowledgments The research was carried out at the Jet Propulsion Laboratory, California Institute of Technology, under a contract with the National Aeronautics and Space Administration (80NM0018D0004).

Conflict of interest The authors declare that they have no conflict of interest.

References

1. H.S. Kim, O.O. Cellek, Z.-Y. Lin, Z.-Y. He, X.-H. Zhao, S. Liu, H. Li, and Y.-H. Zhang, Long-wave infrared nBn photodetectors based on InAs/InAsSb type-II superlattices. *Appl. Phys. Lett.* 101, 161114 (2012). https://doi.org/10.1063/1.4760260.
2. A. Haddadi, G. Chen, R. Chevallier, A.M. Hoang, and M. Razeghi, InAs/InAs$_{1-x}$Sb$_x$ type-II superlattices for high performance long wavelength infrared detection. *Appl. Phys. Lett.* 105, 121104 (2014).
3. A.M. Hoang, G. Chen, R. Chevallier, A. Haddadi, and M. Razeghi, High performance photodiodes based on InAs/InAsSb type-II superlattices for very long wavelength infrared detection. *Appl. Phys. Lett.* 104, 251105 (2014).
4. R. Hao, Y. Ren, S. Liu, J. Guo, G. Wang, Xu. Yingqiang, and Z. Niu, Fabrication and characterization of high lattice matched InAs/InAsSb superlattice infrared photodetector. *J. Crystal Growth* 470, 33 (2017).
5. K. Michalczewski, Ł Kubiszyn, P. Martyniuk, C.H. Wu, J. Jureńczyk, K. Grodecki, D. Benyahia, A. Rogalski, and J. Piotrowski, Demonstration of HOT LWIR T2SLs InAs/InAsSb photodetectors grown on GaAs substrate. *Infrared Phys. Technol.* 95, 222 (2018).
6. E. Delli, V. Letka, P.D. Hodgson, E. Repiso, J.P. Hayton, A.P. Craig, L. Qi, R. Beanland, A. Krier, A.R.J. Marshall, and P.J. Carrington, Mid-infrared InAs/InAsSb superlattice nBn photodetector monolithically integrated onto silicon. *ACS Photon.* 6, 538 (2019).
7. Q. Durlin, J.P. Perez, L. Cerutti, J.B. Rodriguez, T. Cerba, T. Baron, E. Tournié, and P. Christol, Midwave infrared barrier detector based on Ga-free InAs/InAsSb type-II superlattice grown by molecular beam epitaxy on Si substrate. *Infrared Phys. Technol.* 96, 39 (2019).

8. D. Z. Ting, A. Khoshakhlagh, A. Soibel, C. J. Hill, and S. D. Gunapala, Barrier infrared detector, U.S. Patent Application 13/197,588 (2011); U.S. Patent 8,217,480 (2012)
9. David Z. Ting, Alexander Soibel, Arezou Khoshakhlagh, Sam A. Keo, Sir B. Rafol, Anita M. Fisher, Cory J. Hill, Edward M. Luong, Brian J. Pepper, Sarath D. Gunapala, The emergence of InAs/InAsSb type-II strained layer superlattice barrier infrared detectors, SPIEProceedings **11002**, Infrared Technology and Applications XLV; 110020F (2019)
10. E.H. Steenbergen, B.C. Connelly, G.D. Metcalfe, H. Shen, M. Wraback, D. Lubyshev, Y. Qiu, J.M. Fastenau, A.W.K. Liu, S. Elhamri, O.O. Cellek, and Y.-H. Zhang, Significantly improved minority carrier lifetime observed in a long-wavelength infrared III-V type-II superlattice comprised of InAs/InAsSb. *Appl. Phys. Lett.* 99, 251110 (2011).
11. B.V. Olson, E.A. Shaner, J.K. Kim, J.F. Klem, S.D. Hawkins, L.M. Murray, J.P. Prineas, M.E. Flatté, and T.F. Boggess, Time-resolved optical measurements of minority carrier recombination in a mid-wave infrared InAsSb alloy and InAs/InAsSb superlattice. *Appl. Phys. Lett.* 101, 092109 (2012).
12. L. Höglund, D.Z. Ting, A. Khoshakhlagh, A. Soibel, C.J. Hill, A. Fisher, S. Keo, and S.D. Gunapala, Influence of radiative and non-radiative recombination on the minority carrier lifetime in midwave infrared InAs/InAsSb superlattices. *Appl. Phys. Lett.* 103, 221908 (2013).
13. David Z. Ting, Alexander Soibel, Arezou Khoshakhlagh, Sir B. Rafol, Sam A. Keo, Linda Höglund, Anita M. Fisher, Edward M. Luong, and Sarath D. Gunapala, Mid-wavelength high operating temperature barrier infrared detector and focal plane array, Appl. Phys. Lett. **113**, 021101 (2018)
14. D.Z. Ting, S.B. Rafol, K.A. Sam, J. Nguyen, A. Khoshakhlagh, A. Soibel, L. Höglund, A.M. Fisher, E.M. Luong, J.M. Mumolo, J.K. Liu, and S.D. Gunapala, InAs/InAsSb Type-II superlattice mid-wavelength infrared focal plane array with significantly higher operating temperature than InSb. *IEEE Photon. J.* 10, 6804106 (2018).
15. P.C. Klipstein, Y. Livneh, A. Glozman, S. Grossman, O. Klin, N. Snapi, and E. Weiss, Modeling InAs/GaSb and InAs/InAsSb superlattice infrared detectors. *J. Electronic. Mater.* 43, 2984 (2014).
16. I. Vurgaftman, G. Belenky, Y. Lin, D. Donetsky, L. Shterengas, G. Kipshidze, W.L. Sarney, and S.P. Svensson, Interband absorption strength in long-wave infrared type-II superlattices with small and large superlattice periods compared to bulk materials. *Appl. Phys. Lett.* 108, 222101 (2016).
17. D.Z. Ting, A. Soibel, and S.D. Gunapala, Hole effective masses and subband splitting in type-II superlattice infrared detectors. *Appl. Phys. Lett.* 108, 183504 (2016).
18. D.Z. Ting, A. Soibel, and S.D. Gunapala, Type-II superlattice hole effective masses. *Infrared Phys. Technol.* 84, 102 (2017).
19. S. Maimon, and G.W. Wicks, nBn detector, an infrared detector with reduced dark current and higher operating temperature. *Appl. Phys. Lett.* 89, 151109 (2006).
20. P. Klipstein, "XBn" barrier photodetectors for high sensitivity and high operating temperature infrared sensors. *Proc. of SPIE.* 6940, 69402U (2008).
21. D.Z. Ting, A. Khoshakhlagh, A. Soibel, and S.D. Gunapala, Long wavelength InAs/InAsSb infrared superlattice challenges: a theoretical investigation. *J. Elec. Mater.* 49, 6936 (2020).
22. D.E. Sidor, G.R. Savich, and G.W. Wicks, Surface conduction in InAs and GaSb. *Proc. SPIE* 9616, 96160U (2015).
23. D.E. Sidor, G.R. Savich, and G.W. Wicks, Surface leakage mechanisms in III–V infrared barrier detectors. *J. Electronic Materi.* 45, 4663 (2016).
24. S. Maimon, Reduced dark current photodetector, U.S. Patent No. 7,687,871 (2010)
25. P. C. Klipstein, Depletionless photodiode with suppressed dark current and method for producing the same, U.S. Patent No. 7,928,473 (2011)
26. B.-M. Nguyen, S. Bogdanov, S. Abdollahi Pour, and M. Razeghi, Minority electron unipolar photodetectors based on type II InAs/GaSb/AlSb superlattices for very long wavelength infrared detection. *Appl. Phys. Lett.* 95, 183502 (2009).
27. P.C. Klipstein, E. Avnon, Y. Benny et al., Development and production of array barrier detectors at SCD. *J. Electronic. Mater.* 46, 5386 (2017). https://doi.org/10.1007/s11664-017-5590-x.
28. B.T. Marozas, W.D. Hughes, X. Du, D.E. Sidor, G.R. Savich, and G.W. Wicks, Surface dark current mechanisms in III-V infrared photodetectors. *Opt. Mater. Exp.* 8, 1419 (2018).
29. D.Z.-Y. Ting, C.J. Hill, A. Soibel, S.A. Keo, J.M. Mumolo, J. Nguyen, and S.D. Gunapala, A high-performance long wavelength superlattice complementary barrier infrared detector. *Appl. Phy. Lett.* 95, 023508 (2009).
30. D.Z.-Y. Ting, A. Soibel, A. Khoshakhlagh, J. Nguyen, L. Höglund, S.A. Keo, J.M. Mumolo, and S.D. Gunapala, Exclusion, extraction, and junction placement effects in the complementary barrier infrared detector. *Appl. Phys. Lett.* 102, 121109 (2013).
31. D. Z. Ting, A. Soibel, A. Khoshakhlagh, and S. D. Gunapala, Enhanced quantum efficiency barrier infrared detectors, U. S. Patent Application Publication No. US 2019/0013427 A2 (2019); U. S. Patent No. 10,872,987 (2020)
32. D.Z. Ting, A. Soibel, A. Khoshakhlagh, S.A. Keo, A.M. Fisher, S.B. Rafol, L. Höglund, C.J. Hill, B.J. Pepper, and S.D. Gunapala, Long wavelength InAs/InAsSb superlattice barrier infrared detectors with p-type absorber quantum efficiency enhancement. *Appl. Phys. Lett.* 118, 133503 (2021). https://doi.org/10.1063/5.0047937.
33. J.R. Pedrazzani, S. Maimon, and G.W. Wicks, Use of nBn structures to suppress surface leakage currents in unpassivated InAs infrared photodetectors. *Electron. Lett.* 44, 1487 (2009). https://doi.org/10.1049/el:20082925.
34. D.R. Rhiger, and E.P. Smith, Infrared absorption near the bandgap in the InAs/InAsSb superlattice. *Proc. SPIE* 11503, 1150305 (2020). https://doi.org/10.1117/12.2569820.
35. W.E. Tennant, "Rule 07" revisited: still a good heuristic predictor of p/n HgCdTe photodiode performance? *J. Electron. Mater.* 39, 1030 (2010).